Potential Model for Several Mass Anomalies

Associated with Nazca Subduction

by

David Martin

A thesis submitted in partial fulfillment
of the requirements for the degree of

Master of Science

University of Washington

1988

Approved by_____

(Chairperson of Supervisory Committee)

Program Authorized
to Offer Degree_____

Date_____

Master's Thesis

In presenting this thesis in partial fulfillment of the requirements for a Master's degree at the University of Washington, I agree that the Library shall make its copies freely available for inspection. I further agree that extensive copying of this thesis is allowable only for scholarly purposes, consistent with "fair use" as prescribed in the U.S. Copyright Law. Any other reproduction for any purposes or by any means shall not be allowed without my written permission.

Signature_____

Date_____

University of Washington

Abstract

Potential Model for Several Mass Anomalies
Associated with Nazca Subduction

by David Martin

Chairperson of the Supervisory Committee: Professor Robert C. Bostrom
Geophysics Program

A gravitational potential model that employs disk elements is applied to several mass anomalies associated with Nazca subduction. A reasonably good fit to the observed geoid is produced by modeling the trench in conjunction with igneous topography and a uniform anomalous density Nazca slab. Igneous anomalous mass is found to increase with obliqueness of the Nazca plate's motion with respect to strike for the South American subduction zone. A respectable fit to the observed geoid is also made by modeling the trench in combination with a Nazca slab that has lateral density variation, possibly due to variation in the onset of the gabbro-eclogite transition. In this case, subduction inclination angle is found to increase with the anomalous slab density.

Table of Contents

List of Figures

List of Tables

Acknowledgment

The author would like to thank Xu Song. While busy with his own work, he always had time to help me with word processing problems.

Introduction

The process of plate subduction produces a number of mass anomalies. Trenches originate as frictional forces from the underthrusting plate down warp the overriding plate. The resulting sea floor depression defines a relatively long and narrow negative density anomaly. Subduction may produce topographic highs due to tectonic uplift or volcanism. The high areas constitute positive mass anomalies that may, however, be reduced by compensation. Density differences that exist between the subducted slab and the surrounding mantle are assumed to produce a positive net anomalous density. Other anomalies may also be associated with subduction, but their size and structure are not well defined as will be discussed in a following section. A model is then constructed for the Peru-Chile trench, major Andean topography and the subducting Nazca slab (figure 1).

Since gravity and its potential vary as $1/r^2$ and $1/r$ respectively, gravity is relatively more sensitive to surface features [*Chase*, 1979]. The irregular topography of mountainous regions in general and the Andes in particular tends to produce a complex pattern of prominent, short wavelength gravity components [*Grow and Bowin*, 1975]. This situation complicates gravity modeling and therefore mass anomalies are modeled with respect to the geoid. Calculations are also somewhat simplified by dealing with the scalar potential as opposed to the vector gravity field.

Two dimensional gravity models have been made of subduction zone elements for northern Chile [*Grow and Bowin*, 1975]. The Nazca subduction zone has been included in global treatments; *Chase* [1979] has determined the mass anomaly per down-dip length for a number of subducting plates, a slab anomaly model based on plate age has been devised by

Crough and Jurdy [1980] and the open water portion of trenches has been modeled by *Chase and McNutt* [1982]. A detailed model including most of the Nazca subduction zone is sought for a better understanding of its geoid anomalies. Towards this end, a new potential model for subduction zone features is developed.

Figure 1. Idealized west-east cross section through the Chile coast at about 25° S latitude. The Nazca slab (s), Peru-Chile trench (t) and recent volcanic line (v) are shown. The lower boundary of the slab's oceanic crust is indicated by the dashed line.

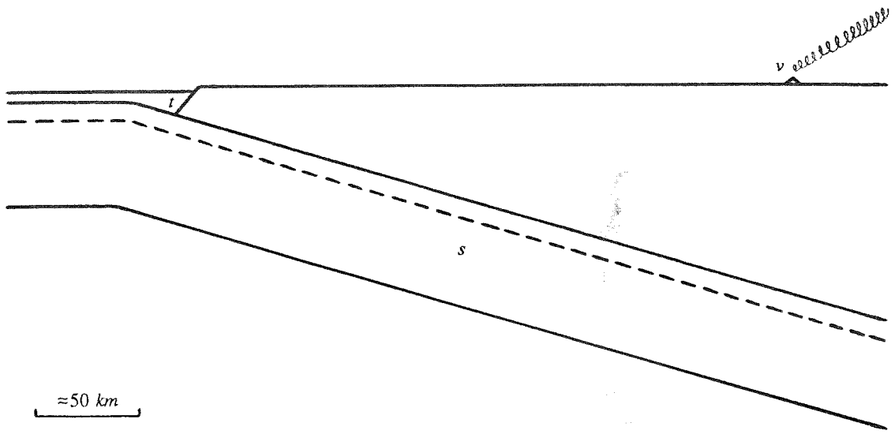
v
t
s
≈50 km

Subducting slabs define a tabular region of anomalous density. As the plate is relatively thin, it will be initially treated as an infinitesimally thin surface with a uniform anomalous areal density [*McAdoo*, 1981]. The cool, dense slab warms at the expense of the surrounding mantle and so the overall thermal anomaly is unchanged [*Hager*, 1984]. The densities of the descending slab and surrounding mantle increase with depth due to thermodynamic changes, but probably not such that the anomalous density is constant [*Schubert et al.*, 1975]. The largest variations in anomalous density probably occur at the locations of phase transitions within the plate. Greater complexity is revealed by the work of *Sung and Burns* [1976] that indicates the sign, in addition to magnitude, of the net mass anomaly produced by olivine to spinel and spinel to oxides transitions may vary with plate velocity. *Schubert et al.* [1975] have these transitions occurring at depths of several hundred kilometers and therefore special consideration is not justified. Several transformations are confined to the oceanic crust (figure 1). The eclogite to garnetite to perovskitite transitions are relatively deep, completed at several hundred kilometers [*Irifune et al.*, 1986], although the gabbro to eclogite phase change could occur at depths of several tens of kilometers [*Ahrens and Schubert*, 1975]. This is probably sufficiently shallow to produce a significant contribution to the plate geoid anomaly. Although the gabbro-eclogite transition will eventually be modeled in terms of spatial distribution, it is not given special treatment in this first model where all density anomalies from phase transformations are simply considered part of the average slab anomaly.

As a first approximation, a simple point element model is tested on a nearly hemispherical shell with uniform density illustrated in figure 2. The shell has the major elements of a typical subducting slab. The high areas have a gentle slope that becomes progressively steeper with increasing depth. Also, the shell has both azimuthal and altitudinal curvature as is the situation for the contorted regions of some slabs. As will become evident, the Nazca slab exhibits prominent examples of this condition. The regular shape of the shell allows for a "fairly" easy calculation of its potential. The potential of any circular symmetric mass distribution can be expressed by a Legendre polynomial expansion [*Ramsey*, 1981]. For the figure 2 shell of radius A and areal density σ_s, the gravitational potential has a closed form only for points on the z axis;

$$U_z = -2\pi A\sigma_s G\left\{ \frac{A}{z} - 1 + \left[1 + \left[\frac{A}{z}\right]^2 - 2\left[\frac{A}{z}\right] cos80° \right]^{½} \right\} \qquad z \geq A$$

Where G is the universal gravitation constant. The radical (square bracket term) is expanded in a Taylor series for $z \rightarrow \infty$ and after rearrangement, the potential becomes;

$$U_z = -2\pi A\sigma_s G\left[(1-c)\left[\frac{A}{z}\right] + \frac{1-c^2}{2}\left[\frac{A}{z}\right]^2 + \frac{c(1-c^2)}{2}\left[\frac{A}{z}\right]^3 + \cdots \right] \qquad z \geq A$$

Here c is defined as $cos80°$. Applying the theorem of Legendre, the general (off axis) expansion is determined to be;

$$U = -2\pi A\sigma_s G\left[(1-c)P_0\left[\frac{A}{\rho}\right] + (1-c^2)\frac{P_1}{2}\left[\frac{A}{\rho}\right]^2 + c(1-c^2)\frac{P_2}{2}\left[\frac{A}{\rho}\right]^3 + \cdots \right] \qquad \rho \geq A$$

The order n Legendre polynomial is represented by $P_n = P_n(cos\phi)$. Although ρ and ϕ orient a general observation location, figure 2 defines these parameters, as used here, in terms of positions on the x axis. A 19 term expansion produces a truncation error of less than 1% at point O on figure 2. For convenience and flexibility a model that positions elements from a regular grid is desirable. The planar point pattern shown in figure 3 is positioned horizontally over the shell such that the O points, axes x and z correspond. The points are then projected vertically downwards onto the shell. Before projection, the mass of each point is $\sqrt{3}\sigma_s B^2/2$ where B is the separation between adjacent points (figure 3). This produces an average areal density of σ_s for the point plane. After projection, the point separation, as measured on shell surface, increases with slope (dip) and so a factor of $1/cos$(dip) is applied to the point masses to maintain an average density of σ_s. The potential (geoid anomaly height) for the shell is calculated at positions along the x axis using the Legendre expansion and the point model (figure 4) where Brun's formula (height = potential/g) is used to express anomaly heights [*Moritz*, 1980]. As would be expected, the point model potential behaves rather badly near points, but it rapidly recovers with increasing distance. This suggests that beyond a critical distance (determined by the number of model elements), the shape of the model element is insignificant.

Disks in a closest packing configuration (figure 3) are used to smooth the potential, especially near the top of the shell. The disk pattern is positioned and projected onto the shell in an analogous manner as for the point case. Disks have the same mass as points ($\sqrt{3}\sigma_s B^2/2$) before projection which corresponds to an individual disk areal density of $2\sqrt{3}\sigma_s/\pi$ so that the disk plane also has an average density of σ_s. After projection, the shell areas between disks increase with dip and therefore a factor of $1/\sqrt{cos(\text{dip})}$ is applied to disk radii (individual disk areal density is unchanged) such that an average density of σ_s is preserved. This method is preferable to varying individual disk densities with constant

radii, since increasing radii with dip improves disk coverage of the shell. A natural advantage of the vertical projection scheme is that shallow areas are modeled with a higher disk frequency than the less critical deeper regions. In an analogous manner as for the shell, the potential of an individual disk of radius R and areal density σ can be expanded in a Legendre series;

$$V = -2\pi R\sigma G\left[\frac{P_0}{2}\left(\frac{R}{r}\right) - \frac{P_2}{8}\left(\frac{R}{r}\right)^3 + \frac{P_4}{16}\left(\frac{R}{r}\right)^5 - \cdots\right] \qquad r \geq R$$

$$V = -2\pi R\sigma G\left[1 - |P_1|\left(\frac{r}{R}\right) + \frac{P_2}{2}\left(\frac{r}{R}\right)^2 - \frac{P_4}{8}\left(\frac{r}{R}\right)^4 + \frac{P_6}{16}\left(\frac{r}{R}\right)^6 - \cdots\right] \qquad r \leq R$$

As before, the universal gravitation constant is G, $P_n = P_n(cos\theta)$ represents the Legendre polynomials and figure 2 defines θ and r in terms of the x axis. Both series are terminated after the last terms shown above. This produces an axial ($\theta = 0$) truncation error at $r = R$ of 9.4% for both expansions. The potential for the disk model is plotted in figure 4. The shell can accomodate a given number of disks (and points) over a limited range of spacing between element centers. With respect to this range, a median potential (for both models) is shown in figure 4. As expected, the model potentials improve with increasing numbers of disks and points. Both models for figure 4 have 96 elements. The disks produce a sufficiently smooth potential and therefore it is this model that is applied to the Nazca plate.

Nazca slab

Subduction occurs along most of the western coast of South America [*Bevis and Isacks*,

1984] as the Nazca plate is thrust under the continent. The Nazca Benioff zone, as determined from teleseismic data by *Bevis and Isacks* [1984], is shown in figure 5. Their preferred surface is not used here for the slab model because it would require a great deal of interpolation between 3° S and 14° S latitude. The only significant difference between the teleseismic and preferred zones occurs around 14° S latitude. *McAdoo* [1981] has shown that the geoid does not reflect relatively small wavelength features in plate geometry. Subduction is especially shallow at around 6° and 32° S latitude (figure 5). *Pilger* [1981] has the shallow subduction in Peru (near 6° S) and northern Chile (near 32° S) due to local low density areas in the Nazca plate associated with the Nazca and Juan Fernandez aseismic ridges respectively. The ridges appear to extend beneath Peru and northern Chile. The Nazca ridge may result from especially thick oceanic crust; thermal expansion of oceanic lithosphere may produce the Juan Fernandez ridge [*Pilger*, 1981]. *Sacks* [1983] attributes the low plate density under Peru to retardation of the basalt (gabbro) to eclogite transformation.

A program (pluto) employing disk elements is developed to model the gravitational potential of the subducting lithosphere. Geoidal effects due to compensated marine and continental topography [*Chase and McNutt*, 1982] are considered small enough to neglect here. Before reaching the subduction zone, the plate is assumed to be in isostatic equilibrium, so that modeling begins at the trench. A grid is constructed over the Benioff zone (figure 5) with 1° separation between disk centers near the equator. The grid orientation is such that strings of disks are nearly parallel to the direction of relative motion for the Nazca plate. The original intent was to produce a model in which slab density could be varied along the subduction direction as may occur for phase changes. This orientation also allows for density variation perpendicular to plate motion as might be expected from changes in plate age along the subduction zone (figure 6) or possible lateral variation in the onset of

the basalt to eclogite transition [*Sacks*, 1983]. As will become evident, modeling errors are relatively large and the geoid is not very sensitive to changes in overall plate depth, so density is not varied in the down-dip direction. Although this initial model has a uniform plate density anomaly, large scale lateral variation is considered in one of the following sections. The disks are projected onto the Benioff zone and pluto adjusts disk parameters in the same manner as for the shell test. A *cos*(latitude) factor is applied to each disk radius to correct for the Mercator projection distortion on figure 5.

Figure 5 contours are for the middle of the Benioff zone and have a depth of 20 *km* at the trench [*Bevis and Isacks*, 1984]. Contour lines for 40 and 60 *km* depths were produced by linear interpolation between the trench and 80 *km* depth line. The subducting lithospere is assumed to have a thickness of 50 *km* [*James*, 1971]. The top of the plate is taken to have an approximately 5 *km* depth at the trench. Pluto then vertically lowers each disk by 10*km*/*cos*(dip) to produce a new surface corresponding to the center of the plate. The dip is calculated in the vicinity of each disk and is also used for adjusting disk radii. Observation points for geoid height calculations are at sea level (in all cases for this paper). For a given observation point, the distance to the center of every disk (r as defined in figure 2) is determined. Also the normal angle (θ in figure 2) is found from the scalar (dot) product of $\vec{r}$ and the normal vector for each disk. These parameters are then used with the truncated disk potential expansions and Brun's formula to calculate the geoid for the point at sea level. As the areal density is used in determining the plate geoid, the plate thickness only influences the depth of the adjusted disk surface. The potential above central areas of the plate should not be very sensitive to moderate changes in overall plate depth, although there may be edge effects, especially near the trench. As an indication of the importance of the uncertainty in plate thickness or location with respect to Benioff zone, the geoid for the 50 *km* plate is compared to that for a plate with a thickness of 80 *km*. At the trench, the center

of the 80 *km* plate is about 50% deeper than the 50 *km* plate center. The *Bevis and Isacks* [1984] Benioff zone (figure 5) is mapped from the trench to a depth of 160 to 300 *km*. By following the trends, this surface is extrapolated to a uniform depth of 320 *km*, so that the adjusted disk surface for the 80 *km* thick plate will have a maximum depth of around 350 *km*. The Benioff zone is also extrapolated 350 *km* to the north of the equator and to the south of 40° S latitude. As the model geoid has the same field as the "observed" geoid in figure 7, all neglected plate mass is at least 350 *km* from points at which the geoid is calculated for the 80 *km* plate. This modification requires a total of 437 disks, 120 of which are produced by the extension. When this 350 *km* extention and common densities are used for the 50 and 80 *km* thick plates, their geoids are not found to be significantly different. These results are shown and discussed in the latter part of this paper.

Creager and Jordan [1984] indicate that some subducting slabs may extend to depths of well over 1000 *km*, although *Anderson* [1987] argues against slab penetration into the lower mantle. It is possible that the Nazca slab (in particular) may not even extend below the seismicity. The deepest portion of the slab will have a low amplitude, long wavelength geoidal expression that is assumed here to be negligible. The problem is in determining at what depth the slab, if present, becomes negligible. The Benioff zone extension is reduced by 100 *km* to produce a 250 *km* extension (relative to the 80 *km* thick plate). This brings the model disk total down to 349 with 46 from extrapolation. As an indication of both extrapolation and plate truncation errors, the 50 *km* plate is modeled with the 250 *km* extension and compared to the 350 *km* results for the same plate thickness. This comparison, with respect to the observed geoid, is made both with and without trench and topographic contributions.

Andes

The western South American geoid (figure 7) is dominated by several somewhat isolated coastal highs [*NASA*, 1982]. A central 56 *m* high lies between two smaller highs of 26 *m* near the equator and 32 *m* at about 33° S latitude. *Liu* [1980] has shown that these relatively short wavelength geoidal highs correspond with the distribution of young South American volcanoes (figure 6). Two volcanic gaps, from 2°-15° and 27°-32° S latitude, divide the volcanoes into three groups [*Morris et al.*, 1979]. *Isacks and Barazangi* [1977] have noted that the gaps occur over areas where subduction is especially shallow (figure 5).

Geoid highs associated with igneous activity may be due to a bulging uplift of the country rock above a magma chamber [*Runcorn*, 1967] or to extruded lava. Whereas the magma chamber itself has a relatively low density and would produce a geoid low [*Runcorn*, 1967], there are a number of examples where the net igneous anomaly is high including the Hawiian Islands, Yellowstone (figure 8) and Iceland [*NASA*, 1982]. Although there is some disagreement as to whether the three South American geoid highs are from igneous activity or tectonic uplift due to subduction, it is initially assumed that their upper portion is not part of the plate anomaly. As will be shown, even a contorted plate, as is the Nazca, cannot produce such short wavelength geoidal features if its anomalous density is approximately uniform to a depth of several hundred kilometers as modeled here. Much of the broad rise around the topographic highs (figure 7) is expected to be from the plate density anomaly. By adjusting the model's anomalous density, a calculated plate geoid can be made to fit the broad rise of the observed geoid. An approximate upper limit for the density can be obtained in this manner. For the plate thickness of 50 *km* with 250 and 350 *km* extensions, the anomalous densities are $8 \pm 1 \times 10^5$ and $7 \pm 1 \times 10^5$ kg/m^2 respectively. The errors are not absolute, but only reflect the modeling difficulty in finding a best-fit.

The plate densities are improved by expanding the model to include what are initially considered to be topographic geoid highs (and eventually the trench). *Liu's* [1980] theory

of an igneous origin for the relatively short wavelength South American geoid highs seems plausible and is therefore used as the basis for the topographic model. Pleistocene glacial rebound studies in northwestern Europe [*Mörner*, 1980] and eastern Canada [*Hillaire-Marcel*, 1980] indicate that mantle compensation response times are on the order of 10^4 *yr*. Therefore only relatively recent igneous activity will produce topographic changes that are as yet uncompensated and so have a significant geoid anomaly. South American volcanoes that have erupted during the last 12000 *yr* (figure 6) are used as an index of recent igneous activity (volcanic and plutonic). Two volcanic data sets corresponding to the plate extensions are considered. One set includes volcanoes from 250 *km* north of the equator to 250 *km* south of 40° S latitude. This produces 14, 27 and 20 volcanoes in the north, central and south groups respectively. The other set has an analogous 350 *km* extension that increases the northern and southern group by two volcanoes each. Both sets include two volcanoes (one in central and south groups) with possible, although somewhat uncertain eruptions during the last 12000 *yr*. A horizontal disk, centered on each volcano, is used to model the anomalous topographic mass in the general vicinity of the volcano. The highest elevation in the Andes is about 7 *km* above sea level [*American Geographical Society*, 1953]. Therefore heights for the centers of anomalous mass in regions defined by the volcanoes are expected to be significantly less than half of this maximum elevation. Such relatively small heights are neglected here and so all disks are positioned at sea level. All disks within any one of the three volcanic groups have the same radius and mass (more convenient than areal density here), although these parameters are adjusted separately for each group. A program (vulcan) calculates the topographic potential from the same Legendre expressions that were used for plate disks. The complete model results are presented after the description of the trench model.

Peru–Chile trench

The Peru-Chile trench extends along much of the western coast of South America [*Prince et al.*, 1980]. The trench is interrupted at around 15° S latitude (figure 6) by the Nazca ridge [*Hayes*, 1966] as this structure is being subducted. The geoidal low expected from the trench manifests itself as "kinks" in the geoid contour lines at the trench vicinity (figure 7). The maximum amplitude of the trench anomaly appears to be at about 11° S latitude.

From the trench bathymetry of *Prince et al.* [1980], the 5 *km* depth contour line is taken to define both the maximum lateral and upper vertical extent of the trench. With respect to this boundary, the trench has an approximately 60 *km* width at its maximum depth of about 3 *km*. The trench is relatively shallow and is therefore modeled by 74 horizontal disks as illustrated in figure 9. Disk radii are varied in accordance with the trench width. Calculated geoid heights (in all cases) are made at regular 1° intervals in both latitude and longitude. Since the trench has a maximum width of about .6° (great circle), it is relatively narrow with respect to the output grid. This implies that the element shape is unimportant and that inadequacies in disk coverage of the trench are negligible as long as mass is conserved.

A program (charon) is developed to calculate the trench geoid. The trench is assumed to have a triangular cross section (figure 9) that has a constant (average) area over the extent of any given disk. Each disk then corresponds with a trench volume that is defined by a triangular right cylinder. Therefore the depth to the center of anomalous mass for any of the 74 trench segments will be less than or equal to 1 *km* (1/3 maximum depth) with respect to the 5 *km* reference level. As in the case of the topography, relatively small vertical distances are neglected and all trench disks are placed 5 *km* below sea level. Sediments in the trench vicinity have an assumed density of 2600 kg/m^3 [*Grow and Bowin*, 1975] so that the anomalous density is about -1600 kg/m^3 (sea water minus sediment density). Charon deter-

mines the anomalous trench mass (negative) associated with each disk and, using the previous disk potential expansions (as truncated for the plate model), calculates the resulting trench contribution to the geoid (figure 10). The lowest point on the trench geoid is about -7 *m*. Compared to overall height ranges of the observed geoid (figure 7), the trench influence appears to be relatively small, although *Cazenave et al.* [1986] indicate that lows of down to -20 *m* may be associated with some trenches. Only the open water portion of the trench is modeled, so that any uncompacted sediments within the trench will increase the anomaly [*Cazenave et al.*, 1986]. *Chase and McNutt's* [1982] combined model of compensated topography (continental and marine) and uncompensated open water trench anomalies produces a maximum low of between -5 and -10 *m* near the Peru-Chile trench, although only the long wavelength (≥1800 *km*) geoid is considered.

Whereas the ocean side trench boundary is fairly well defined by the 5 *km* depth level, the continental side has no obvious trench boundary (idealized *a-b* cross section of figure 9). Rather than having the open water upper boundary represented by a horizontal plane, a surface that slopes upward toward the coast would probably be more realistic. The problem is that the slope of such a surface would be arbitrarily designated. Therefore, the horizontal surface is used here as a lower limit for the open water upper boundary. This situation will most likely produce a calculated trench geoid anomaly that is too small in an approximately uniform manner over its lateral extent. In contrast, the somewhat patchy nature of neglected uncompacted trench sediments [*Kulm et al.*, 1977] results in a calculated anomaly that may be locally smaller than the actual trench anomaly. In light of these conditions, the figure 10 anomaly is regarded as a minimum limit (in the positive sense) for the trench.

Complete model

A best-fit to the observed geoid is obtained by adjusting the plate anomalous density in conjunction with the radius and mass for volcanic groups in combination with the trench geoid. Figure 11 shows the best-fit geoid for the 350 *km* extension with plate thickness of 50 *km*. Both line trend and elevation were considered in the fitting process. The line kinking from the trench is evident, but has significantly reduced amplitude near 11° S latitude when compared to figure 7. Lateral contour line displacements near 11° S latitude indicate a trench anomaly at or below -7 *m* for the observed geoid, whereas the anomaly is about half this value for the corresponding region of the calculated trench geoid (figure 10). Sediments in the Peru portion of the trench [*Kulm et al.*, 1977] having relatively high porosity may be responsible. The overall character of the topographic highs is in good agreement with those in figure 7. Greater detail could be produced by adjusting the mass and radius for individual volcanoes, but little is probably gained from doing so. The broad plate high between volcanoes and to the southeast compares well for figures 7 and 11, but not as well in the northeast due to an unmodeled low (-58 *m*) near the West Indies. The best-fit (for 350 *km* extension and 50 *km* thickness) plate and topographic contributions to the geoid are separately displayed in figures 12 and 13. For the figure 12 plate geoid, contour lines that are nearly parallel over most of the field tend to converge at the far northern and southern regions. This is only partly due to effects from lateral truncation of the plate. The greater plate dip that occurs near 0° and 40° S latitude (figure 5) also contributes to the lower geoid heights in these areas. The 350 *km* cutoff as related to volcanic modeling, appears to have very little influence on the topographic geoid (figure 13).

Results for the adjustable parameters of the figure 11 geoid and the two previously described tests are compiled in table 1. As expected, variation in plate thickness is relatively unimportant, producing no change in plate density and only minor changes in the parameters for the north and south volcanic groups. The 80 *km* thick plate geoid (350 *km*

extension) as shown in figure 14 does not differ significantly from that for a 50 *km* plate thickness (figure 12) with the same density and extension. The complete geoid including trench, topography and plate based on a 250 *km* extension appears in figure 15. The 100 *km* reduction for the plate and volcano extensions results in a 25% plate density increase with respect to the 350 *km* extension and small changes for the north and south volcanoes. The difference in plate density is at about the modeling error ($\pm 1 \times 10^5$ kg/m^2) for this parameter. Extending the plate and volcanoes to 450 *km* will certainly produce a significantly smaller change, although much greater extensions may not. In light of this, $4 \pm 1 \times 10^5$ kg/m^2 will be considered (temporarily) an upper bound for the average anomalous plate density. For a 50 *km* thick Nazca slab, this density corresponds to an average volume density of 8 kg/m^3, although thermal boundaries become indistinct as heat from surrounding mantle conducts into the plate [*Toksöz et al.*, 1971].

Using *McKenzie's* [1969] thermal slab model, as modified by *Molnar and Gray* [1979], *Chase* [1979] calculates a linear anomalous density of 3.6×10^{12} kg/m of down-dip slab length for the Nazca plate extending to a 325 *km* depth. Assuming the lateral length of South American subduction is 6.4×10^6 *m* [*Chase*, 1979], here the linear is converted to an areal density of 5.6×10^5 kg/m^2. The model accounts for plate heating due to adiabatic compression [*McKenzie*, 1970], but the thermal anomaly produced in the surrounding mantle and slab heating from phase changes (latent) and friction [*Toksöz et al.*, 1971] are not considered. Direct density changes due to phase transitions are also neglected. This density is not far above the upper limit found here, although the calculation is based on a 100 *km* plate thickness which may be too large for the Nazca slab [*James*, 1971].

A least square fit to the observed geoid (minus calculated trench geoid) is also used to determine the 50 *km* thick plate anomalous density and the three group volcanic masses for the 350 *km* extension. Results are stated in the last row of table 1 and plotted in figure 16

(with trench). The field grid is the same as was used for previous calculations (1° intervals) and although this produces an overall greater weight for geoid heights in the southern region due to meridian convergence, no other weights are imposed. The density and masses are simultaneously fit in the least square sense with respect to the height residuals. The residuals (figure 17) in the vicinity of volcanoes, especially around the central group, could probably be significantly reduced by individually least square fitting the volcanic disk masses. Relative to modeling errors and approximations for the plate and trench, such detailed topographic modeling does not seem justified. In comparison to the trial and error method, least squares produces a smaller plate density and larger topographic masses, although residuals are not greatly reduced. The mean absolute residuals (for the 861 point fields) are 5.8 and 5.7 *m* for the trial-error and least square fits respectively. To a certain extent, geoidal effects due to a change in plate density may be somewhat offset by an opposite change in the topographic masses. Since geoid contour line trends are not considered, the least square mass for the southern volcano group is especially high (table 1, figure 16). The depressed region (from West Indies low) in the upper right portion of the observed geoid (figure 7) produces the largest least square residuals (figure 17) and would contribute to the lower least square plate density. Under these circumstances, the least square fit serves as an approximate check on the previous results, although the trial and error parameters for the 50 *km* plate thickness and 350 *km* extension (table 1, second row) are considered the most representative values for the plate density and topographic masses.

The calculated geoid field is relatively large and therefore pluto, vulcan and charon were written to account for the curvature of the earth. This significantly increases the model's mathematical complexity and therefore lengthens computation time. In retrospect, this was probably not necessary, since at distances for which the earth's curvature becomes important, the geoid contribution is not.

As subduction occurs, the overriding plate may be depressed due to viscous drag from the underthrusting plate [*Davies*, 1981]. *McAdoo* [1982] has used this effect to constrain non-Newtonian mantle flow. The sinking slab can also produce a viscous distortion of internal (subsurface) density boundaries. From this condition, in conjunction with surface depression, *Hager* [1984] has set mantle viscosity constraints for a Newtonian rheology. The model presented here disregards these effects. Since the viscous distortions have the same overall geometry as the subducting slab, they produce a geoid low with essentially the same spectral content (spherical harmonic) and lateral shape as the plate high. Moreover the amplitude of the low appears to depend, in part, on mantle conditions that are poorly understood. It is therefore practically impossible to separate the distortion low from the plate geoid high. What was previously regarded as an upper limit for plate anomalous density (4×10^5 kg/m^2) may be too low. Since the plate high and distortion geoid low are essentially indistinguishable, the model indirectly accounts for the low in so much as it may be considered part of the overall plate anomaly. In any case, topography parameters, which are the main concern here, are more accurate as a result of the plate model and unaffected by uncertainty in the distortion geoid low amplitude.

Table 1. Best-fit plate and topography results

Extension * (*km*)	Plate thickness (*km*)	Plate anomalous density (10^5 *kg*/m^2)	Group volcano mass (10^{15} *kg*), radius (*km*) north	central	south
350	80	4	8, 50	60, 300	9, 80
† 350	50	4	7, 50	60, 300	9, 90
‡ 250	50	5	8, 60	60, 300	9, 100
§ 350	50	2.3	9.4, 50	64, 300	16, 90

* explained in text

† corresponding geoid is plotted in figure 10

‡ geoid is plotted in figure 14

§ density and masses from least square fit, with geoid plotted in figure 15

Figure 2. Section of a spherical shell with radius A and areal density σ_s, that is used to test potential models. One point and disk of radius R are shown on the shell surface. The angle θ is between the disk normal and r.

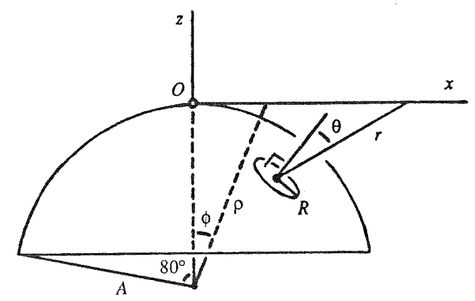
z
O
x
θ
r
R
ρ
ϕ
80°
A

Figure 3. Closest packing disk and corresponding point pattern (continues in all directions). The distance between adjacent points and disk centers is B. The z axis is out of the page. Point O, axes x and z are as in figure 2.

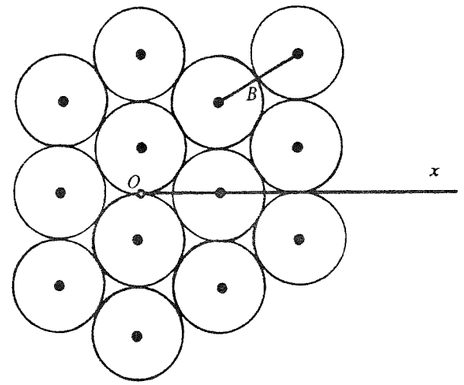
B
O
x

Figure 4. Geoid anomaly height for figure 2 shell with areal density σ_s and radius A, calculated by 19 term Legendre expansion (*e*), disk (*d*) and point (*p*) models. Both models use 96 elements (points and disks) with a distance of .1918A between element centers (B in figure 3) before projection onto the shell. The acceleration and universal constant of gravity are g and G respectively.

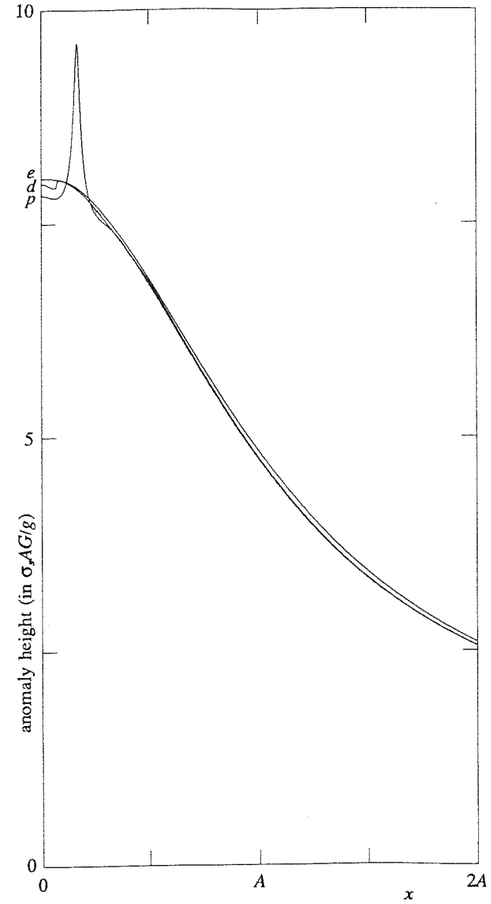
10
5
0
e
d
p
anomaly height (in $\sigma_s AG/g$)
0
A
2A
x

Figure 5. Part of the disk grid (with some disks) used to cover the subducting plate. The arrow approximates the Nazca plate's relative direction of motion [*Minster and Jordan*, 1978]. Depth contours (in kilometers to middle of Benioff zone) and earthquakes (small disks) are from *Bevis and Isacks* [1984]. The line of solid disks are fictional hypocenters located 20 *km* beneath the trench and were used as a boundary for determining the best-fitting surface [*Bevis and Isacks*, 1984]. All longitudes (figures 5-20) are western and except where indicated, latitudes (figures 5-7, 9-20) are southern. (Mercator projection)

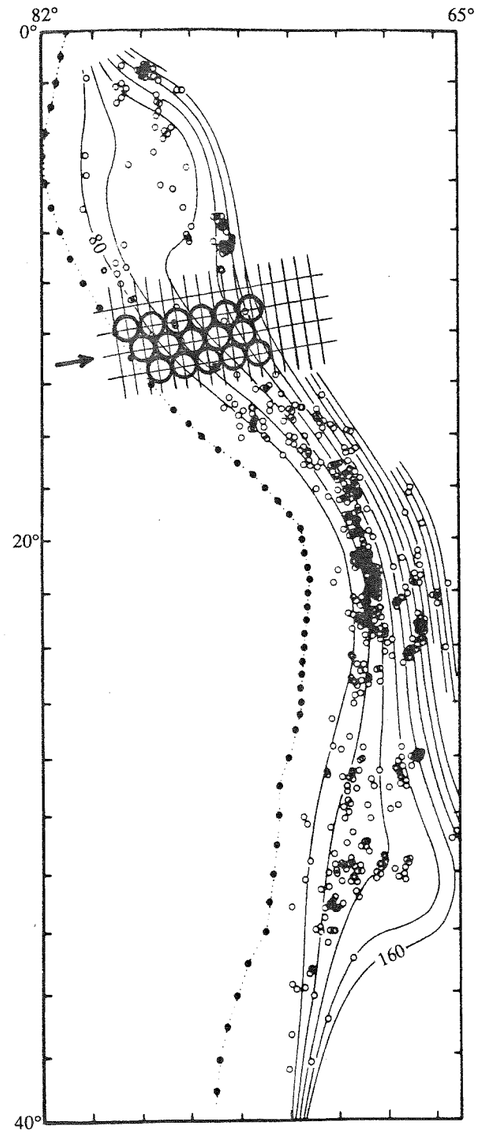
82°
65°
0°
80
20°
160
40°

Figure 6. Andean volcanoes that have erupted during the last 12000 *yr* (circumflexes) after *Morris et al.* [1979], Nazca plate sea floor ages [*Larson et al.*, 1985] and the Peru-Chile trench (dark areas) approximately defined here by the 5 *km* depth contour from *Prince et al.* [1980]. Dashed lines are approximately parallel to plate motion and define the south group (volcano) and south gap plate sections. (simple cylindrical projection)

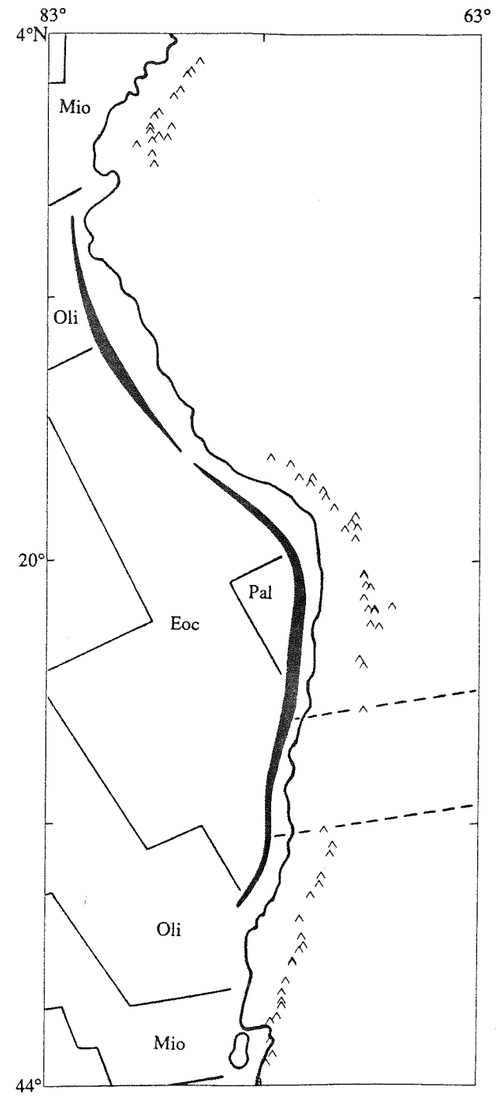
83°
63°
4°N
Mio
Oli
20°
Pal
Eoc
Oli
Mio
44°

Figure 7. The geoid over western South America, adapted from *NASA* [1982]. The contour interval is 2 *m*. For all geoids (figures 7, 8, 10-20) the projection is simple cylindrical.

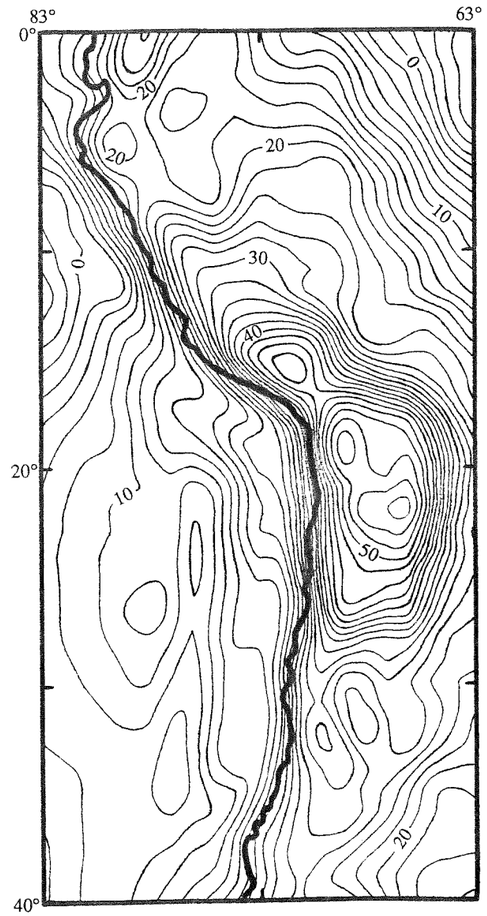
83°
63°
0°
20°
40°
0
20
20
20
30
40
10
0
10
50
20

Figure 8. The geoid near west-central North America, adapted from *NASA* [1982]. The thrust symbol indicates the approximate location and extent of Juan de Fuca subduction, after *Taber and Smith* [1985]. The Yellowstone high is in the east-central portion of the field. (latitudes are northern)

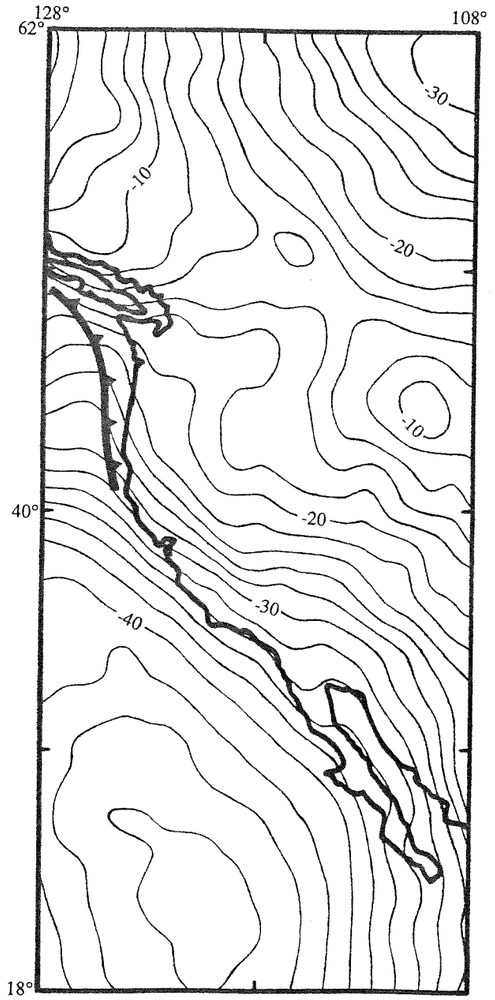
128°
108°
62°
40°
18°
-10
-20
-30
-40
-10
-20
-30

Figure 9. Two of the 74 disks used to model the Peru-Chile trench as defined by the 5 *km* depth contours adopted from *Prince et al.* [1980]. An idealized triangular cross section (*a-b*), with about a factor of ten vertical exaggeration, appears in the upper right corner (dashed line is at 5 *km* depth). The greatest trench depth at the cross section is 1.0 *km* with respect to the 5 *km* reference level. This depth with the approximate trench width and disk diameter (length of triangular prism) are used to calculate the trench volume associated with the large disk. (Mercator projection)

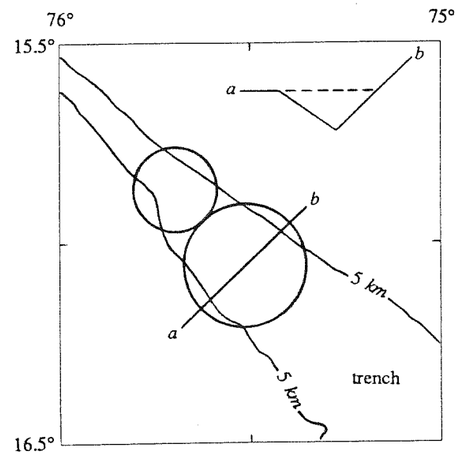
76°
75°
15.5°
16.5°
a
b
b
a
5 km
5 km
trench

Figure 10. The trench geoid anomaly with a 1 *m* contour interval. All geoid heights (figures 10-20) are calculated at "rectangular" 1° intervals in latitude and longitude.

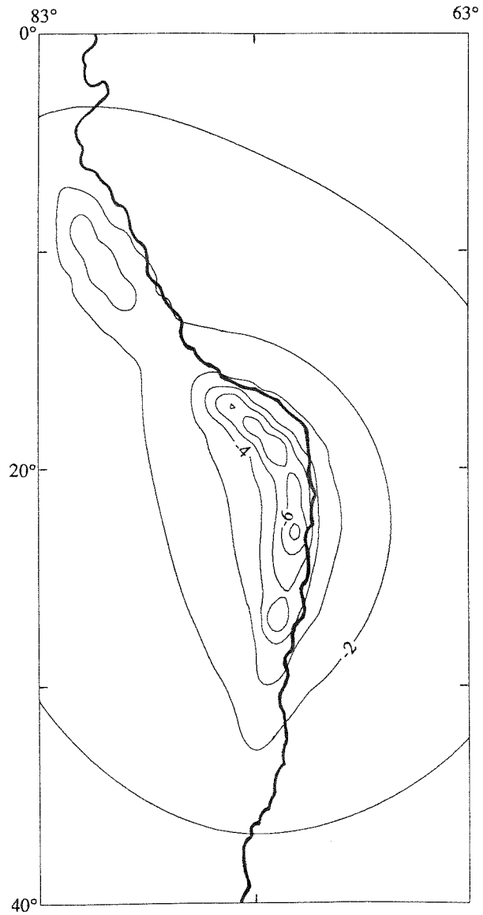
83°
63°
0°
20°
40°
4
6
2
1

Figure 11. The complete (trench, plate, topography) calculated geoid for the 350 *km* extension (described in text) and plate thickness of 50 *km*, contoured at 2 *m* intervals. The corresponding adjusted parameters are listed in the second row of table 1.

Figure 11. The complete (trench, plate, topography) calculated geoid for the 350 *km* extension (described in text) and plate thickness of 50 *km*, contoured at 2 *m* intervals. The corresponding adjusted parameters are listed in the second row of table 1.

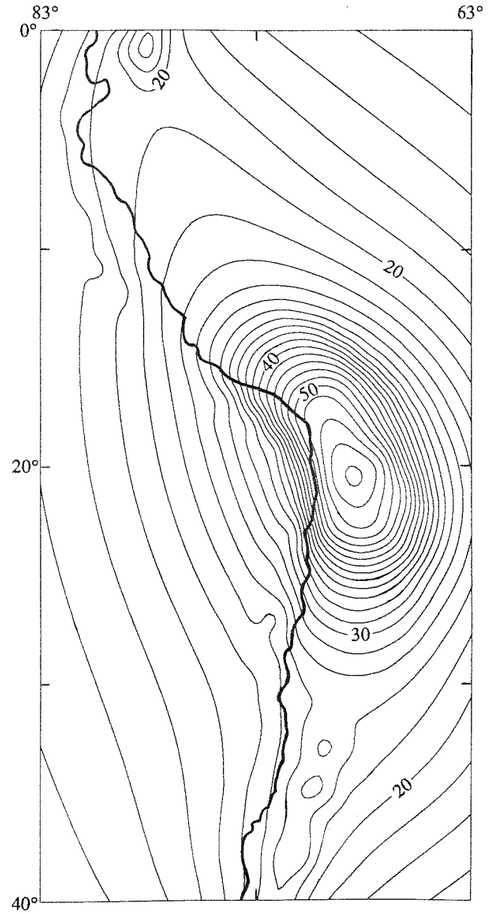
83°
63°
0°
20°
40°
20
20
40
50
30
20

Figure 12. The plate geoidal anomaly for 50 *km* thickness and 350 *km* extension as for figure 11. Contour interval is 1 *m*.

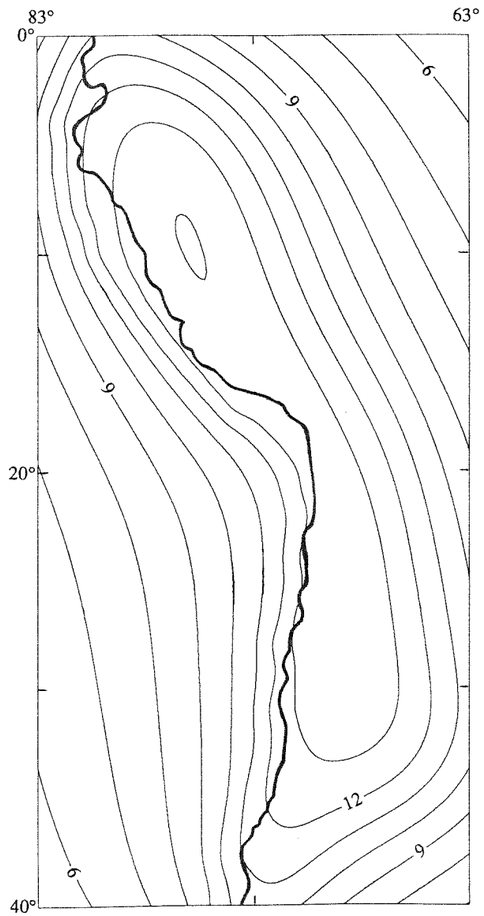
83°
63°
0°
20°
40°
6
9
12

Figure 13. The geoid anomaly due to major continental topography, modeled by volcanism corresponding to the 350 *km* extension (best-fit with 50 *km* thick plate) as for figure 11. The contour interval is 2 *m*.

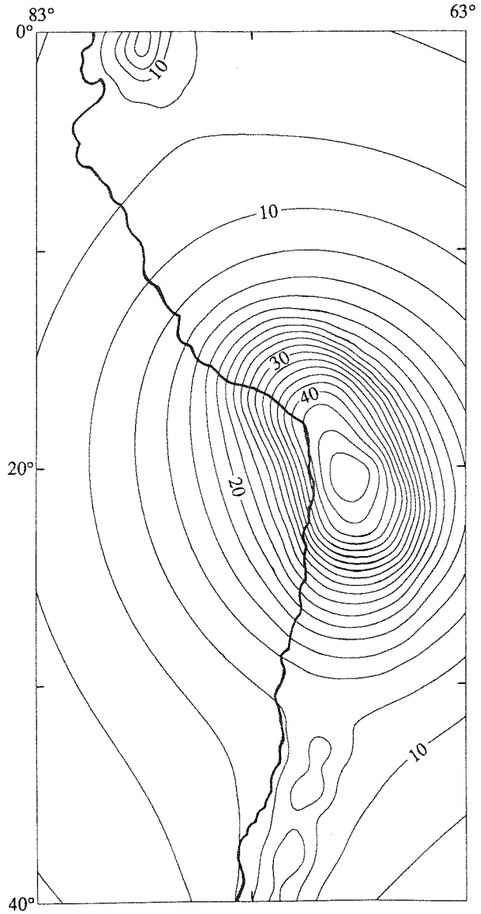
83°
63°
0°
20°
40°
10
10
30
40
20
10

Figure 14. The plate geoidal anomaly for 80 *km* thickness and 350 *km* extension with a 1 *m* contour interval. The plate density is the same as for figure 12.

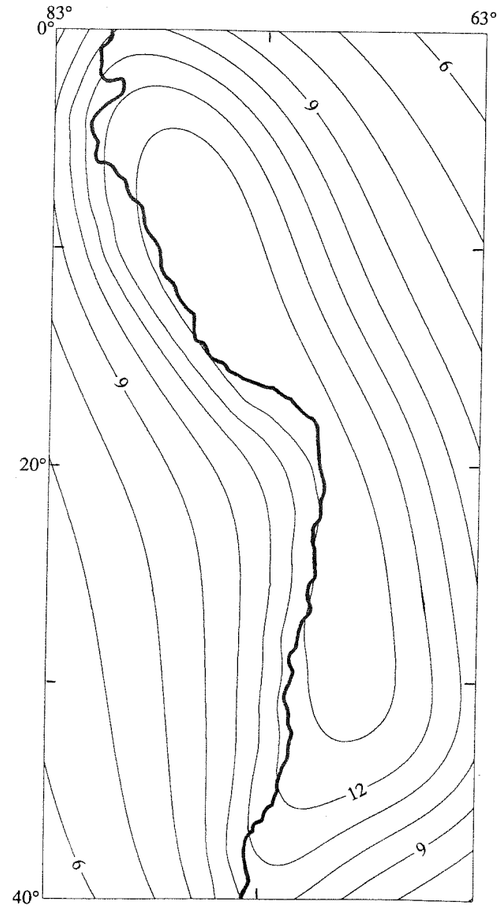
0°
83°
63°
20°
40°
6
9
12
9
6

Figure 15. The complete (trench, plate, topography) calculated geoid for the 250 *km* extension and plate thickness of 50 *km*, contoured at 2 *m* intervals. Adjusted parameters are listed in the third row of table 1.

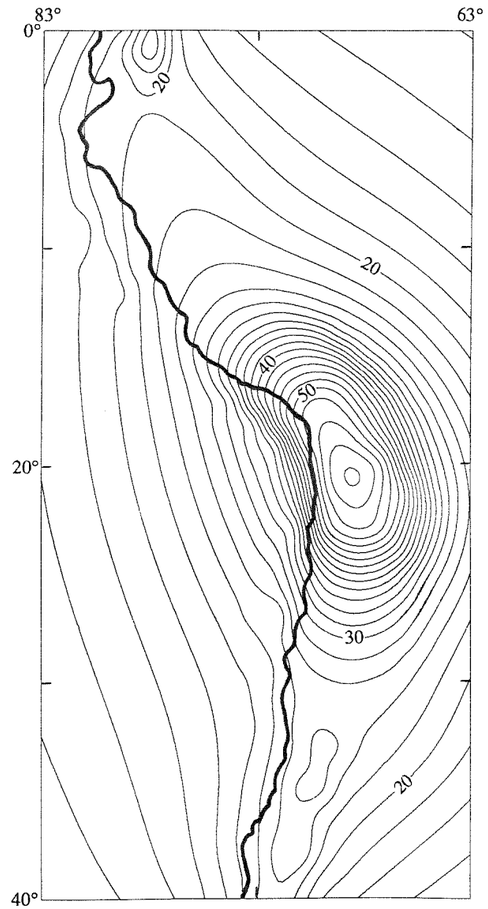
83°
63°
0°
20°
40°
20
20
40
50
30
20

Figure 16. The complete (trench, plate, topography) least square geoid for 350 *km* extension and 50 *km* plate thickness, contoured at 2 *m* intervals. Corresponding parameters appear in the last row of table 1.

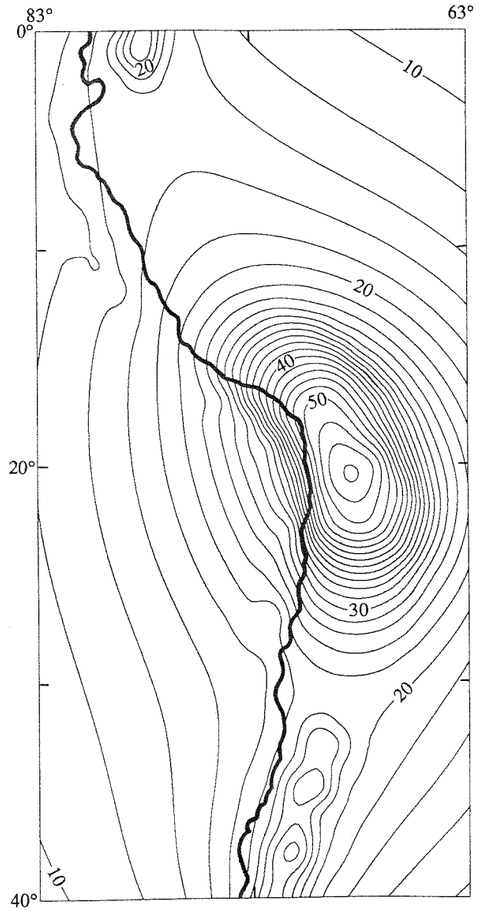
83°
63°
0°
20°
40°
10
20
40
50
30
20
10

Figure 17. Least square residuals for 50 *km* plate thickness and 350 *km* extension as for figure 16. The contour interval is 2 *m*.

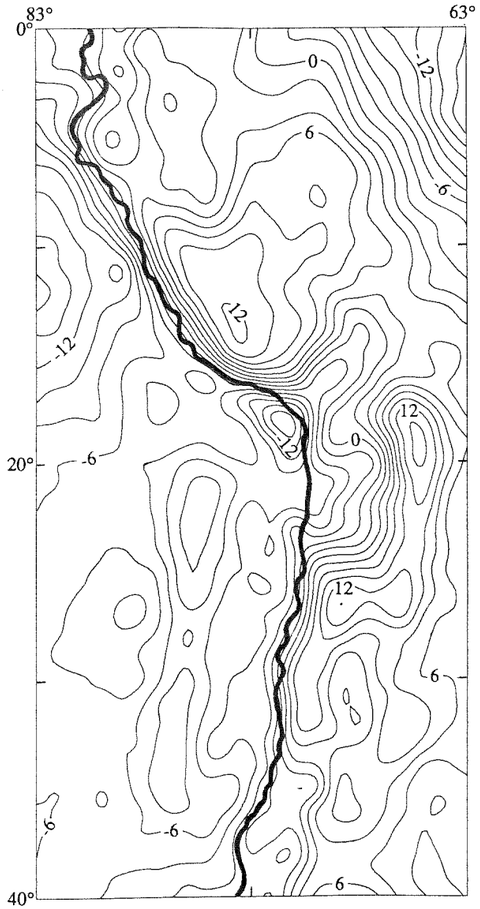
83°
63°
0°
20°
40°
0
6
-6
-12
12

Discussion

Chase and McNutt [1982] have calculated the combined geoid contribution from topography (continental and marine) that is assumed to be completely compensated and the open water anomaly of uncompensated trenches. Under this condition, most of South America produces a topographic geoid of 5 to 10 *m* with the highest anomaly at between 10 and 15 *m* occurring in the general region of the central volcano group. The figure 12 topographic geoid indicates that topography in association with young volcanoes is far from being in isostatic equilibrium. The simple Bouguer anomaly for west-central South America [*Ocola and Meyer*, 1973] is strongly negative (several hundred milligals) in the vicinity of the central volcanoes. Therefore the central group is at least partially compensated to a significant extent. The height of a total anomalous mass slab (equivalent rectangular parallelepiped) is determined for each volcanic group. The slabs are as long as each volcanic line and have widths corresponding to the disk diameters for each group. Rock density is assumed to be 2700 kg/m^3 which is approximately the density of andesite [*Johnson and Olhoeft*, 1984]. The corresponding heights are found to be .7, .7 and .3 *km* for north, central and south groups respectively, with masses and radii from the second row of table 1 (350 *km* extension, 50 *km* thickness). This is a reasonable result as much of the area covered by the volcanic disks is higher than 2 *km* above sea level [*American Geographical Society*, 1953]. An order of magnitude calculation can be made for the minimum growth rate for topography assuming a mantle compensation response time of approximately 10^4 *yr*. For about one vertical kilometer of uncompensated topography, the rate must be greater than $1km/10^4yr$ or 10 *cm/yr*. Within an order of magnitude, this is not an unrealistic rate for igneous or tec-

tonic processes.

The volcanic/plutonic hypothesis for geoid highs in South America is consistent with the general behavior of igneous activity. From thermal considerations, *Abbott and Hoffman* [1984] have suggested that older subducting lithosphere produces larger volumes of magma. For the three Andean groups, the anomalous mass and radius per volcano (table 1) increase with plate age at the trench (figure 6). The highest point on the observed geoid (figure 7) corresponds to the oldest (Paleocene) plate section. In regard to the Juan de Fuca (Farallon) plate, *Verplanck and Duncan* [1987] have shown that volcanic activity, as indicated by volcanic rock thicknesses, increases with subduction rate as determined by the relative velocity magnitude and obliqueness. Where subduction rate is the plate relative velocity component perpendicular to the continental margin. The loss of plate volatiles and therefore magma production is affected by the normal relative velocity [*Verplanck and Duncan*, 1987]. This result is tested for South American subduction. Using *Minster and Jordan's* [1978] parameters (relative rotation rate and pole), the relative Nazca plate velocity (magnitude and direction, neglecting dip) is calculated at the location of each volcano and averages are found for each group. The average strike of a group volcanic line is determined by a linear regression for the coordinates (latitude and longitude) of its volcanoes. Obliqueness is defined here as the average angle between the plate motion direction and volcanic strike. For the north, central and south volcanic groups, obliqueness and average velocity magnitude are found to be 50°, 80°, 65° and 8.1, 9.2, 9.2 *cm/yr* respectively. From these results, plate velocity components normal to the volcanic strike are 6.2, 9.1 and 8.3 *cm/yr* for north to south groups. Group mass and radius (table 1) increase with normal subduction rate. Although the geoid is adequately modeled by using the volcanic scheme, igneous activity may not be appropriately represented by the anomalous mass and radius as indexed by individual volcanoes (table 1, last columns). Plutonic uplift and lava volumes may vary sub-

stantially for volcanoes in different groups. The extent of igneous activity is perhaps more accurately expressed by the average linear anomalous density as determined by dividing the total anomalous mass by the length of the volcanic line for any given group. This produces linear densities of .2, 1 and .2 $\times 10^{12}$ *kg/m* for the north, central and south groups from the 350 *km* extension and 50 *km* plate thickness (table 1, second row). The northern and southern volcanic groups are not distinguished (within modeling error), although their corresponding plate ages do not greatly differ. This result is also generally consistent with the findings of *Verplanck and Duncan* [1987].

The South American volcanic gaps suggest a relationship for igneous activity. Shallow subduction under the gaps may produce relatively small volumes of high silica and therefore high viscosity magma from partial plate melting at relatively low pressure [*Abbott and Hoffman*, 1984]. The low volume and high viscosity magma will tend to crystallize before reaching the earth's surface and so volcanism does not result. This same process, operating to a variable extent, could be responsible for the differences in igneous activity for the volcanic groups as indicated by the geoid. Deep pluton emplacement will have little effect on the short wavelength topographic geoid highs. As a test of this possibility, plate (top surface) depths are calculated beneath each volcano within the field of figure 5 and averaged for each group. This field size reduces the north group to 9 and the south group to 15 volcanoes (central is unchanged at 27). The north group requires Benioff zone contour line extrapolation (figure 5) for 5 volcanoes (there is no extrapolation for central and south groups). Depths determined from the mid-seismic Benioff zone contours in figure 5 are corrected to the top of the plate by subtracting 15*km*/*cos*(dip). The Benioff zone dip is found in the vicinity of each volcano. Average depths of 190, 120 and 90 *km* are calculated for the north, central and south groups. These and previous other parameters possibly related to group igneous activity are collected in table 2. Although the depth for the north

group is poorly constrained near the equator (figure 5), plate depth does not seem to be the primary cause of anomalous mass variation between volcanic groups. Normal velocity components (table 2) predict a smaller linear density for the north as compared to the south group (both are at 2×10^{11} *kg/m*). Relatively large amounts of low viscosity magma produced by the greater plate depth for the north group may be enough to neutralize, but not reverse the velocity effect in this case. Plate depth as related to igneous activity may be more of a critical, all or none, phenomenon. The ends of the lower northern, upper central and southern volcanic group lines are abrupt (figure 6). Only the lower end of the central group shows any gradational thinning; this occurs at the gap edge over the most gradual transition from shallow to "normal" subduction (figure 5). It seems that volcanism is very sensitive, in an absolute, on or off sense, to plate depth variation along the direction of volcanic strike.

Cascades

A more convincing argument could be made by relating plate velocity or possible age to igneous activity for another subduction zone. As other factors may also influence igneous activity, a subduction zone with the same general character as the South American zone is preferred for comparison. Anomalous igneous mass at or near the earth's surface may depend on the type of overriding plate (oceanic or continental) and on the underthrusting plate dip angle which may influence the depth of magma production [*Abbott and Hoffman*, 1984]. For Juan de Fuca (figure 8) and Nazca (figure 5) subduction, an oceanic plate is thrusting under a continent at a relatively shallow angle. Although Juan de Fuca (here including Explorer and Gorda) subduction is essentially aseismic in British Columbia and Oregon [*Crosson and Owens*, 1987], Benioff zones have been profiled in northern California [*Walter*, 1986] and mapped in Washington [*Crosson and Owens*, 1987]. Other methods

used to locate the slab, including seismic reflection [*Green et al.*, 1986], *P* wave dispersion [*Michaelson and Weaver*, 1986], *P* wave conversion [*Langston*, 1981] and volcanic petrology [*Dickinson*, 1970], also generally indicate shallow subduction.

The geoid in the Juan de Fuca subduction zone vicinity (figure 8) is largely controlled by a major low (-46 *m*), located around 15° S of California, and to a lesser extent by highs over Yellowstone and in Alaska [*NASA*, 1982]. Because of this complication, in addition to the absence of an open water trench and laterally continuous Benioff zone, the model used for South America is not applied here. Since the trench is filled with sediment [*Silver*, 1969], perhaps in part from the Columbia river, a relatively small trench anomaly is anticipated (no major rivers flow into the Pacific from South America [*American Geographical Society*, 1953]). The slight geoid depression that parallels the Oregon coast (figure 8) may be produced by low density sediment in the trench. There are a number of young volcanoes [*Morris et al.*, 1979] associated with Juan de Fuca subduction, but there is essentially no geoid expression for anomalous igneous or plate mass.

Volcanoes erupting during the last 12000 *yr* extend along the coast from southeastern Alaska to northern Mexico in an irregular, but roughly continuous band that spreads eastward across west-central and southwestern United States [*Morris et al.*, 1979]. Juan de Fuca plate volcanism is not well defined relative to the Nazca situation. The volcanic strike (Juan de Fuca) is approximately (and somewhat arbitrarily) defined by a line intersecting Mt. Baker in northern Washington and Mt. Lassen in northern California. Using magnetic sea floor anomalies, *Riddihough* [1977, 1980] has determined recent (average for last million years) relative velocity vectors for the Juan de Fuca plate. From these results, volcanic strike normal components of .3, 2.7, 2.3 and -.5 *cm/yr* are calculated for the Explorer, central, Gorda northern and southern sections of the Juan de Fuca plate (from north to south). The Juan de Fuca plate, as defined here, appears to be composed of at least three separate

plates [*Riddihough*, 1977, 1980] with the southern Gorda unit actually moving away from the volcanic line. All four normal components are significantly less than any of those for the Nazca plate (smallest 6.2 *cm/yr* for north group). Plate ages along the Juan de Fuca subduction zone are Quaternary, Pliocene and Miocene [*Larson et al.*, 1985]. These ages are generally younger than those for any of the Nazca plate volcanic groups (table 2). Since the Juan de Fuca plate produces a negligible anomalous igneous mass, the velocities and ages are consistent with trends found for South American subduction.

Gabbro–eclogite transition

Although a Nazca plate with nearly uniform anomalous density produces a relatively broad geoid high (figure 12), perhaps lateral variation in plate density, instead of igneous topography, could be used to model the short wavelength (high) anomalies over South America. Differences in anomalous density along the plate strike could result from variation in the depths of phase transformations, especially as for gabbro to eclogite as discussed earlier. Anomalous density changes could be significant as typical densities of gabbro and eclogite range from 2900 to 3100 and 3400 to 3500 kg/m^3 respectively [*Ahrens and Schubert*, 1975]. *Sacks'* [1983] hypothesis for subduction under the northern volcanic gap (Peru) is also assumed for the southern gap; shallow subduction results locally from a relatively low plate section density produced by retardation of the gabbro-eclogite transition. The volcanic distribution (recent), which is rather sensitive to depth, is used to define five Nazca plate sections. The last volcano at the lower end of the north group, both central group ends and the upper end of the south group, defines section boundaries which are constructed nearly parallel to plate motion. The two dashed lines in figure 6 border the south gap and south group plate sctions. Similar boundaries define the north group, north gap and central group plate sections. The 350 *km* extension (and 50 *km* plate thickness) is used here so that

the north and south group sections extend 350 *km* above the equator and below 40° S latitude respectively. Plate anomalous densities are uniform within sections, but allowed to vary from one section to another.

A least square fit to the observed geoid (minus calculated trench geoid) is used to determine the areal anomalous densities for the five plate sections. Results are listed in table 3 and plotted in figure 18. As before, the field grid has 1° intervals and no weights (other than produced by meridian convergence) are applied. As in the previous volcano-plate fit, large residuals (figure 19) are produced in the northeastern area of the field due to the West Indies low. The mean absolute residual is 6.4 *m* for sections, which is not much greater than that for the volcano-plate fit (5.7 *m*). A better fit could undoubtedly be made by using more plate sections, but little is probably gained from doing so. On figure 19, a zero height contour nearly coincides with the coastline such that areas over the continent have residual highs of magnitudes that approximate those expected from compensated topography (with uncompensated open water trench) as determined by *Chase and McNutt* [1982].

Neglecting contributions from compensated topography, a somewhat better fit can be made to the short wavelength geoid highs by trial and error adjustment of plate densities with less emphasis on the outlying areas (long wavelengths), especially near the West Indies low. These results are shown in table 3 and figure 20. The upper portions of the central (group) high and southern ridge are in fairly good agreement with the observed geoid (figure 7), but the mean absolute residual now becomes 7.9 *m*. The northern high remains poorly defined, although the corresponding plate section's (north group) geometry is not well defined by earthquakes near the equator (figure 5).

As a general test of the gabbro-eclogite retardation theory [*Sacks*, 1983], plate section densities are assumed to be related to subduction inclination angles. *Ahrens and Schubert* [1975] suggest that this transition may influence the subduction process. For the mid-

seismic zone of figure 5, the average subduction angle (horizontal reference) is found between the trench (20 *km* depth) and 160 *km* depth (deepest laterally continuous contour). The angle is given by *arctan*(140*km*/*L*) where *L* is the horizontal distance between the trench and depth of 160 *km*. For the figure 5 field (with no extrapolation), average angles are determined at 1° (great circle) intervals along the trench, approximately parallel to the direction of plate motion. Mean angles are found for each plate section (table 3). Section angles and least square densities are plotted in figure 21. The trial and error densities are not plotted because, although they provide a better geoid fit in the vicinity of the short wavelength highs, the gap plate sections are difficult to adjust objectively. Also, unlike the volcano model, the plate sections produce all of the short and long wavelength highs and therefore long wavelengths cannot be neglected. Figure 21 shows an evident relation between density and angle if the north group plate section is discarded. This section's mean angle is only determined from two average angles (28.7°, 19.3°), the largest of which is nearest the equator and not well constrained by earthquakes (figure 5). The north group section has a relatively high fraction of extrapolated disks (16 of 24). Also, the West Indies low will tend to produce a lower density for the north group section and therefore disregarding this section seems justified.

Here, as for the previous model (volcano-plate), anomalous section densities are probably somewhat inaccurate due to plate truncation. It is assumed that all section densities would be decreased, by a nearly constant term, from the inclusion of the neglected (if present) lower portion of the Nazca plate. The angle-density relation of figure 21 would be generally preserved as only the ordinate intercept should be affected.

As before, viscous distortions (other than the trench) associated with the subducting slab have not been given special treatment and are considered part of each plate section anomaly. The assumption made here is that the geoid anomaly low due to viscous distortion

will be approximately uniform along the strike of the subduction zone as the magnitude of the relative subduction velocity does not show much lateral variation for South America (8.1, 9.2, 9.2 *cm/yr* averages for north, central, south volcanic groups). Therefore as in the case of truncation, the distortion low will not affect density-angle correlation, but only the ordinate intercept of figure 21, although in the opposite direction; section densities may be too low by a constant term (related to viscous distortion).

The previous arguments indicate that differences between section areal densities should not be significantly affected by viscous distortion or plate truncation. Least square section anomalous densities have a range of about 2.5×10^6 kg/m^2 (-.071 to 2.4×10^6 kg/m^2). Assuming this variation is due to the gabbro-eclogite transition and therefore confined to the plate crust, the corresponding anomalous crustal volume density range is approximately 300 kg/m^3 for a crust thickness of about 9 *km* as determined by *Fisher and Raitt* [1962]. This is not an unreasonable result as it is less than the difference in density between eclogite and gabbro which is around 500 kg/m^3.

Geoid low anomalies due to viscous distortions may also be related to the slab inclination angle. Since density variations within the earth have (essentially) only radial dependence, plates that are subducting nearly horizontally may produce viscous distortions, but the distortions (lateral) will not result in density anomalies. This effect would tend to produce higher overall densities for the combined plate and distortion anomaly of shallow (subducted) sections, whereas just the opposite is indicated in figure 21. Therefore the density-angle correlation cannot be explained by this effect.

Table 2. Group igneous activity parameters

Volcanic group	Linear mass anomaly (10^{12} *kg/m*) *	Plate normal velocity (*cm/yr*) †	Plate (top) depth (*km*) ‡	Plate age along trench §
north	.2	6.2	190	Mio, Oli
central	1	9.1	120	Eoc, Pal
south	.2	8.3	90	Mio, Oli, Eoc

* from group parameters for 350 *km* extension and 50 *km* plate thickness, table 1, row 2

† averages for 350 *km* extension volcanoes with respect to volcanic strike

‡ averages for figure 4 field volcanoes (no extension)

§ corresponding to 350 *km* extension volcanoes

Table 3. Plate section parameters

Plate section *	Model disks † total, extrapolated	Density (10^5 kg/m^2) ‡ least square, trial-error	Inclination angle § number, mean
north group	24, 16	7.9, 10	2, 24.0°
north gap	139, 35	1.1, .9	14, 12.4°
central group	102, 7	24, 30	14, 19.4°
south gap	53, 8	-.71, -.4	5, 13.7°
south group	119, 54	5.7, 9	8, 15.7°

* with respect to volcanic distribution as described in text

† for plate sections corresponding to the 350 *km* extension and 50 *km* plate thickness

‡ least square and trial-error geoids are plotted in figures 18 and 19 respectively

§ determined at 1° (great circle) intervals along trench for mid-seismic zone as explained in text

Figure 18. The complete (trench, plate sections) least square geoid for 350 *km* extension and 50 *km* plate thickness, contoured with a 2 *m* interval. Corresponding parameters are listed in the third column (first position) of table 3.

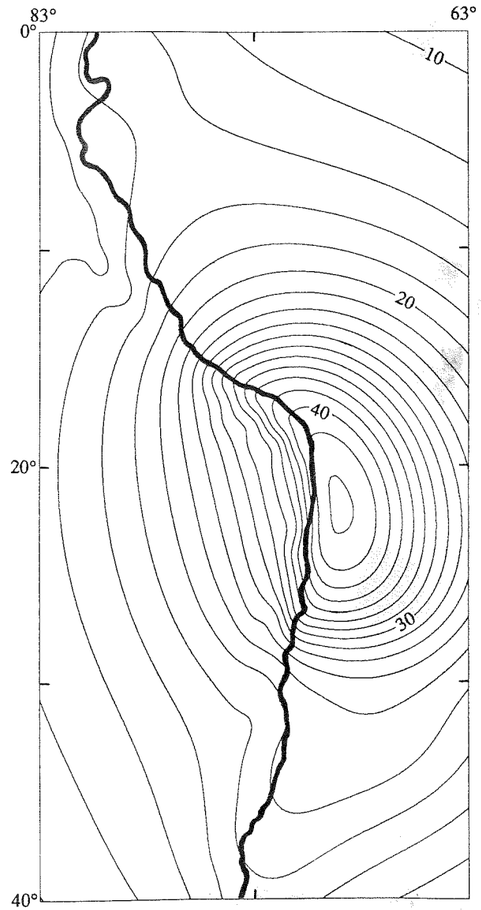
83°
63°
0°
20°
40°
10
20
30
40

Figure 19. Least square section residuals for 50 *km* plate thickness and 350 *km* extension as for figure 18. The contour interval is 2 *m*.

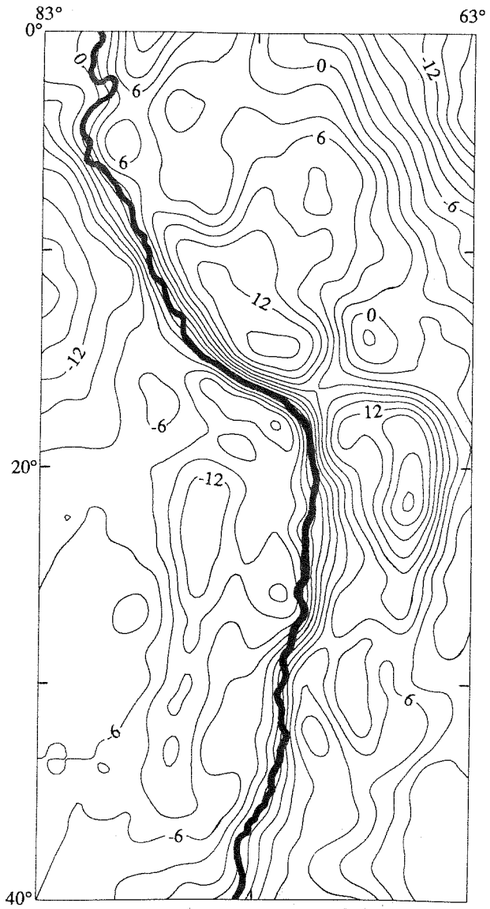
83°
63°
0°
20°
40°
0
6
-6
12
-12

Figure 20. The complete (trench, plate sections) trial and error geoid for 350 *km* extension and 50 *km* plate thickness, contoured at 2 *m* intervals. Adjusted parameters appear in the third column (second position) of table 3.

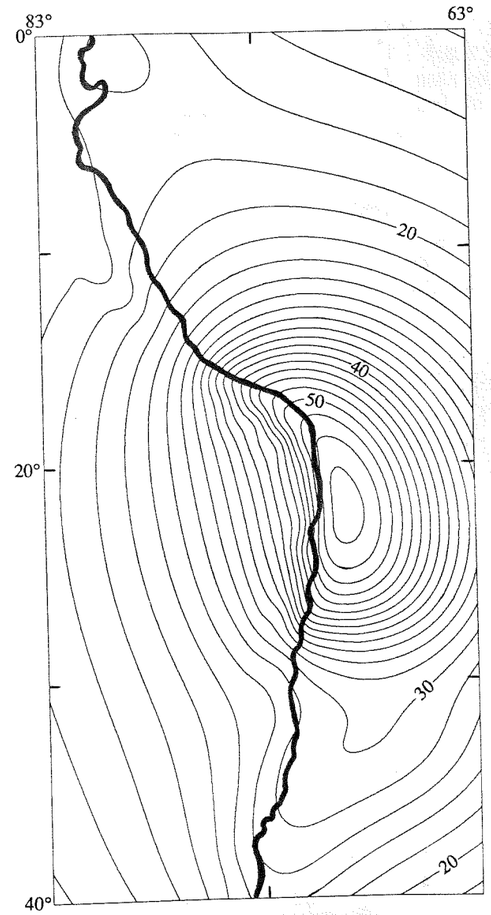
0°
83°
63°
20°
40°
20
40
50
30
20

Figure 21. Plot of least square average anomalous density versus the mean subduction inclination angle for plate sections. Data are from columns three (first position) and four (second position) of table 3. The linear regression line does not include the point represented by the circle (north group section) for reasons discussed in text.

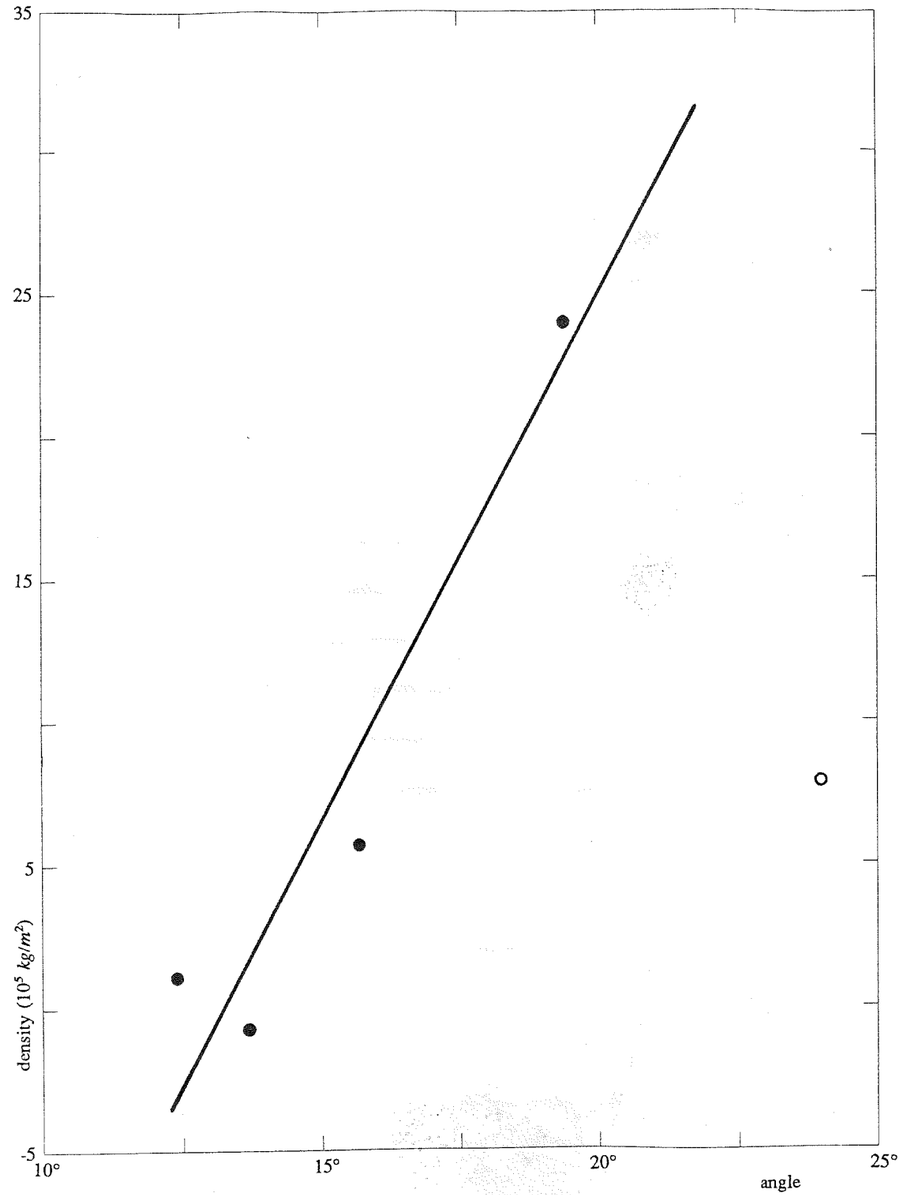
35
25
15
5
-5
density (10^5 kg/m^2)
10°
15°
20°
25°
angle

Conclusion

The disk gravitational potential model is found to be sufficiently accurate, flexible and fast. Speed is especially important for the plate program which performs several hundred thousand individual element potential calculations for each geoid field. Although, in general, gravitational potential inversion does not produce a unique density distribution, the models used here are at least spatially constrained to a certain extent.

The trench portion of the observed South American geoid appears to be only partially explained by the open water anomaly as defined by ther boundaries used here. Upward variation from the horizontal top surface (open water) boundary (used here) and relatively low density uncompacted sediments within certain segments of the Peru-Chile trench may substantially contribute to the trench geoid low. For a uniform anomalous areal density, the subducting Nazca plate is found to produce a long wavelength geoid high that is relatively insensitive to moderate uncertainty in overall plate depth as affected mostly here by plate thickness.

Uncompensated topography may be responsible for a significant portion of the geoid height in western South America and may substantially contribute to other subduction zone geoids. For the New Hebrides and Tonga-Kermadec zones, *McAdoo's* [1981] slab model falls 12 and 16 *m* short of two observed geoid highs. The missing, relatively short wavelength portion of the geoid may be due to unmodeled topography of the young volcanic island chains [*Morris et al.*, 1979] associated with subduction. Igneous activity seems to be an adequate basis for modeling the short wavelength geoid highs in South America. Volcanic gaps (recent) that divide the Andes into three distinct groups make this area ideal

for study of igneous activity. For the Cascades and Andean volcanic groups, igneous activity, as indicated by anomalous mass, is found to increase with normal subduction rate and plate age. Depth of magma production may be a contributing factor, but does not seem to be the prime cause of anomalous topographic mass variation at subduction zones. Although these findings are only based on four volcanic lines, the corresponding parameters (table 2) that have been considered here are effectively averaged over relatively large distances.

Alternatively, the short wavelength South American geoid highs can also be explained by lateral variation in plate density (with no topographic contribution). Lateral variation in depth of the gabbro-eclogite transition may produce changes in anomalous plate density along the strike of the subduction zone. Such density variation may influence the subducting plate's geometry; inclination angle is found to increase with anomalous density for the Nazca slab.

Cocos subduction, along the southwestern coast of southern Mexico and Central America, suggests possible future work. The subducting plate appears to split into two distinct sections; the north and south plate sections have relatively shallow and steep dips respectively [*Bevis and Isacks*, 1984] so that model plate density comparisons might be made. A moderate, but separate geoid high appears over each of the two slabs [*NASA*, 1982], although several nearby anomalies, including the low south of California (figure 8), tend to complicate the region. Some of these surrounding anomalies would probably need to be modeled first to provide a background for modeling anomalies associated with Cocos subduction. Since northern Cocos subduction has the same character as the Nazca and Juan de Fuca zones (shallow oceanic plate subduction under a continent), it could also be used for igneous topographic model comparisons. Few other subduction zones fit these criteria. Volcanism is well defined for the northern Cocos segment and consists of a string of about

nine young volcanoes (last 12000 *yr* eruptions) as indicated by *Morris et al.* [1979]. Cocos zone models might help to indicate whether igneous topographic mass or the plate density anomaly is a more important factor in producing geoid highs over continental subduction zones.

Bibliography

Abbott, D. H., and S. E. Hoffman, Archaean plate tectonics revisited 1. heat flow, spreading rate, and the age of subducting oceanic lithosphere and their effects on the origin and evolution of continents, *Tectonics, 3,* 429-448, 1984.

Ahrens, T. J., and G. Schubert, Gabbro-eclogite reaction rate and its geophysical significance, *Reviews of Geophysics and Space Physics, 13,* 383-400, 1975.

American Geographical Society, South America, from *Atlas of the Americas,* New York, 1953.

Anderson, D. L., Thermally induced phase changes, lateral heterogeneity of the mantle, continental roots and deep slab anomalies, *Journal of Geophysical Research, 92,* 13968-13980, 1987.

Bevis, M., and B. L. Isacks, Hypocentral trend surface analysis: probing the geometry of Benioff zones, *Journal of Geophysical Research, 89,* 6153-6170, 1984.

Cazenave, A., C. Rosemberg-Borot, and M. Rabinowicz, Geoid lows over deep-sea trenches, *Journal of Geophysical Research, 91,* 1989-2003, 1986.

Chase, C. G., Subduction, the geoid, and lower mantle convection, *Nature, 282,* 464-468, 1979.

Chase, C. G., M. K. McNutt, The geoid: effect of compensated topography and uncompensated oceanic trenches, *Geophysical Research Letters, 9,* 29-32, 1982.

Creager, K. C., and T. H. Jordan, Slab penetration into the lower mantle, *Journal of Geophysical Research, 89,* 3031-3049, 1984.

Crosson, R. S., and T. J. Owens, Slab geometry of the Cascadia subduction zone beneath Washington from earthquake hypocenters and teleseismic converted waves, *Geophysical Research Letters, 14,* 824-827, 1987.

Crough, S. T., D. M. Jurdy, Subducted lithosphere, hotspots and the geoid, *Earth and Planetary Science Letters, 48,* 15-22, 1980.

Davies, G. F., Regional compensation of subducted lithosphere: effects on geoid, gravity and topography from a preliminary model, *Earth and Planetary Science Letters, 54,* 431-441, 1981.

Dickinson, W. R., Relations of andesites, granites, and derivative sandstones to arc-trench

tectonics, *Reviews of Geophysics and Space Physics, 8,* 813-860, 1970.

Fisher, R. L., and R. W. Raitt, Topography and structure of the Peru-Chile trench, *Deep-Sea Research, 9,* 423-443, 1962.

Green, A. G., R. M. Clowes, C. J. Yorath, C. Spencer, E. R. Kanasewich, M. T. Brandon, A. Sutherland Brown, Seismic reflection imaging of the subducting Juan de Fuca plate, *Nature, 319,* 210-213, 1986.

Grow, J. A., and C. O. Bowin, Evidence for high-density crust and mantle beneath the Chile trench due to descending lithosphere, *Journal of Geophysical Research, 80,* 1449-1458, 1975.

Hager, B. H., Subducted slabs and the geoid: constraints on mantle rheology and flow, *Journal of Geophysical Research, 89,* 6003-6015, 1984.

Hayes, D. E., A geophysical investigation of the Peru-Chile trench, *Marine Geology, 4,* 309-351, 1966.

Hillaire-Marcel, C., Multiple component postglacial emergence, eastern Hudson Bay, Canada, in *Earth Rheology, Isostacy and Eustasy,* edited by N.-A. Mörner, pp. 215-230, John Wiley, London, 1980.

Irifune, T., T. Sekine, A. E. Ringwood, and W. O. Hibberson, The eclogite-garnetite transformation at high pressure and some geophysical implications, *Earth and Planetary Science Letters, 77,* 245-256, 1986.

Isacks, B. L., and M. Barazangi, Geometry of Benioff zones: lateral segmentation and downwards bending of the subducted lithosphere, in *Island Arcs, Deep Sea Trenches and Back-Arc Basins,* edited by M. Talwani, and W. C. Pitman III, pp. 99-114, American Geophysical Union, Washington, D. C., 1977.

James, D. E., Plate tectonic model for the evolution of the central Andes, *Geological Society of America Bulletin, 82,* 3325-3346, 1971.

Johnson, G. R., and G. R. Olhoeft, Density of rocks and minerals, in *CRC Handbook of Physical Properties of Rocks, Volume III,* edited by R. S. Carmichael, pp. 1-38, CRC Press, Boca Raton, Florida, 1984.

Kulm, L. D., W. J. Schweller, and A. Masias, A preliminary analysis of the subduction processes along the Andean continental margin, 6° to 45° S, in *Island Arcs, Deep Sea Trenches and Back-Arc Basins,* edited by M. Talwani and W. C. Pitman III, pp. 285-301, American Geophysical Union, Washington, D. C., 1977.

Langston, C. A., Evidence for the subducting lithosphere under southern Vancouver Island and western Oregon from teleseismic *P* wave conversions, *Journal of Geophysical Research, 86,* 3857-3866, 1981.

Larson, R. L., W. C. Pitman III, X. Golovchenko, S. C. Cande, J. F. Dewey, W. F. Haxby, and J. L. LaBrecque, *The Bedrock Geology of the World,* W. H. Freeman and Company,

New York, 1985.

Liu, H.-S., Mantle convection pattern and subcrustal stress field under South America, *Modern Geology, 7,* 161-169, 1980.

McAdoo, D. C., Geoid anomalies in the vicinity of subduction zones, *Journal of Geophysical Research, 86,* 6073-6090, 1981.

McAdoo, D. C., On the compensation of geoid anomalies due to subducting slabs, *Journal of Geophysical Research, 87,* 8684-8692, 1982.

McKenzie, D. P., Speculation on the consequences and causes of plate motions, *The Geophysical Journal of the Royal Astronomical Society, 18,* 1-32, 1969.

McKenzie, D. P., Temperature and potential temperature beneath island arcs, *Tectonophysics, 10,* 357-366, 1970.

Michaelson, C. A., and C. S. Weaver, Upper mantle structure from teleseismic *P* wave arrivals in Washington and northern Oregon, *Journal of Geophysical Research, 91,* 2077-2094, 1986.

Minster, J. B., and T. H. Jordan, Present day plate motions, *Journal of Geophysical Research, 83,* 5331-5354, 1978.

Molnar, P., and D. Gray, Subduction of continental lithosphere: some constraints and uncertainties, *Geology, 7,* 58-62, 1979.

Moritz, H., *Advanced Physical Geodesy,* p. 14, Abacus Press, Tunbridge Wells, England, 1980.

Mörner, N.-A., The Fennoscandian uplift: geological data and their geodynamical implications, in *Earth Rheology, Isostasy and Eustasy,* edited by N.-A. Mörner, pp. 251-284, John Wiley, London, 1980.

Morris, L. D., T. Simkin, and H. Meyers, *Volcanoes of the World,* National Oceanic and Atmospheric Administration, 1979.

NASA, *GEM 10B 1° × 1° Geoid,* National Aeronautics and Space Administration, 1982.

Ocola, L. C., and R. P. Meyer, Crustal structure from the Pacific basin to the Brazilian shield between 12° and 30° south latitude, *Geological Society of America Bulletin, 84, 3387-3404, 1973.*

Pilger, R. H., Plate reconstructions, aseismic ridges, and low-angle subduction beneath the Andes, *Geological Society of America Bulletin, Part I, 92,* 448-456, 1981.

Prince, R. A., A. Masias, G. L. Shepherd, G. E. Ness, W. T. Coulbourn, and W. J. Schweller, *Bathymetry of the Peru-Chile Trench and Continental Margin Latitude 3°–40° South,* Geological Society of America, 1980.

Ramsey, A. S., *Newtonian Attraction,* p. 131, Cambridge University Press, Cambridge, England, 1981.

Riddihough, R. P., A model for recent plate interactions off Canada's west coast, *Canadian Journal of Earth Sciences, 14,* 384-396, 1977.

Riddihough, R. P., Gorda plate motions from magnetic anomaly analysis, *Earth and Planetary Science Letters, 51,* 163-170, 1980.

Runcorn, S. K., Flow in the mantle inferred from the low degree harmonics of the geopotential, *The Geophysical Journal of the Royal Astronomical Society, 14,* 375-384, 1967.

Sacks, I. S., The subduction of young lithosphere, *Journal of Geophysical Research, 88,* 3355-3366, 1983.

Schubert, G., D. A. Yuen, and D. L. Turcotte, Role of phase transitions in a dynamic mantle, *The Geophysical Journal of the Royal Astronomical Society, 42,* 705-735, 1975.

Silver, E. A., Late Cenozoic underthrusting of the continental margin off northernmost California, *Science, 166,* 1265-1266, 1969.

Sung, C.-M., and R. G. Burns, Kinetics of high-pressure phase transformations: implications to the evolution of the olivine→spinel transition in the downgoing lithosphere and its consequences on the dynamics of the mantle, *Tectonophysics, 31,* 1-32, 1976.

Taber, J. J., and S. W. Smith, Seismicity and focal mechanisms associated with the subduction of the Juan de Fuca plate beneath the Olympic peninsula, Washington, *Bulletin of the Seismological Society of America, 75,* 237-249, 1985.

Toksöz, M. N., J. W. Minear, and B. R. Julian, Temperature field and geophysical effects of a downgoing slab, *Journal of Geophysical Research, 76,* 1113-1138, 1971.

Verplanck, E. P., and R. A. Duncan, Temporal variations in plate convergence and eruption rates in the western Cascades, Oregon, *Tectonics, 6,* 197-209, 1987.

Walter, S. R., Intermediate-focus earthquakes associated with Gorda plate subduction in northern California, *Bulletin of the Seismological Society of America, 76,* 583-588, 1986.